ADVANCED MATERIALS TECHNOLOGIES
www.advmattechnol.de

Heterogeneous Conductance-Based Locally Shape-Morphable Soft Electrothermal Actuator

Junseong Ahn, Yongrok Jeong, Zhi-Jun Zhao, Soonhyoung Hwang, Kyuyoung Kim, Jiwoo Ko, Sohee Jeon, Jaeho Park, Hyeokjung Kang, Jun-Ho Jeong, and Inkyu Park**

The development of soft electrothermal actuators (ETAs) that can be designed in arbitrary shapes and can easily handle soft objects has recently attracted much attention. However, the existing ETAs cannot be locally designed with a single substrate geometry, which places certain limitations on their applications. In addition, some limited materials (e.g., highly aligned carbon nanotubes) are used as heating layers for improving actuation controllability, which results in a high driving voltage, thus limiting the diversity and utility of ETAs. Herein, a novel method for a heterogeneous conductance-based locally shape-morphable electrothermal actuator (HC-ETA) is suggested, revealing that conductance programming allows control of the heat distribution in ETAs. Thus, by controlling the actuator heat distribution, the designed actuation motion can be implemented. Furthermore, Ag nanowire/carbon nanotube composites are used as conductive nanomaterials for a heating layer to realize a low-driving-voltage actuator. Additionally, combining a porous fabric substrate with a bipolymer actuator structure allows mechanical interlocking and the chemical bonding between actuator multilayers, resulting in significantly enhanced mechanical durability. Finally, the utility of the proposed actuator and the corresponding design method is successfully demonstrated by fabricating a biomimetic self-walking robot and an object lifting soft robot for vacuum chamber applications.

1. Introduction

Recently, soft actuators have attracted much attention in view of the increasing need for healthcare- and manufacturing-related robots, artificial muscles, and micromanipulators. Compared to conventional rigid actuators, soft actuators are more appropriate for human–machine interactions and use in wearable devices, as they can handle soft materials and arbitrary shapes.[1–3] Soft actuators can be driven by mechanical,[4,5] optical,[6–9] chemical,[10] magnetic,[11–13] and electrical[14,15] stimuli but need to be actuated with an easily accessible power source for practical applications. Among them, electrical stimuli provided by electroactive and field-activated polymers such as electro-driven hydrogels[16] and ionic polymer–metal composites (IPMCs)[17] are considered to be the most suited for this purpose. However, electro-driven hydrogels can be used only in electrolyte-containing environments, and IPMCs feature a short-range working stroke. Thus, recent research has focused on electrically stimulated actuators driven by Joule heating rather than by direct electrical stimulation, as exemplified by shape memory polymers (SMPs)[18] and electrothermal actuators (ETAs).[19,20] SMPs exhibit the disadvantages of limited material and actuation shape diversity, as they are driven by two-stage discontinuous deformation of a specific polymer over its transition temperature. Therefore, ETAs, which are driven by bending due to the coefficient of thermal expansion (CTE) difference of a bimorph structure, have been actively studied because of advantages such as light weight, being electrolyte-free, actuation simplicity, and continuous shape change.

However, despite these rapid ETA developments, some problems such as the low diversity of actuation shapes still remain. In order for an actuator to be used in various fields, it should exhibit a broad diversity of controllable shapes. Most previous studies in this area have focused on actuator shape control based on the design of an electrical path comprising anisotropic properties of aligned materials.[21,22] Unfortunately, this approach requires the use of highly aligned nanomaterials and complex electrical paths, which limits the material scope and increases the driving voltage. Alternatively, the shape diversity problem has been solved by attachment of stiff materials[23] on some parts or by making use of the anisotropic expansion of an actuation material.[24,25] However, the design diversity needs to be increased further, as expansion directions cannot be locally controlled with a single substrate geometry, and the attachment of stiff materials does not allow for continuous shape actuation.

J. Ahn, K. Kim, J. Ko, Dr. J. Park, Prof. I. Park
Department of Mechanical Engineering
Korea Advanced Institute of Science and Technology (KAIST)
Daejeon 34141, Republic of Korea
E-mail: inkyu@kaist.ac.kr

J. Ahn, Y. Jeong, Dr. Z.-J. Zhao, Dr. S. Hwang, J. Ko, Dr. S. Jeon, H. Kang, Dr. J.-H. Jeong
Department of Nano Manufacturing Technology
Korea Institute of Machinery and Materials (KIMM)
Daejeon 34103, Republic of Korea
E-mail: jhjeong@kimm.re.kr

The ORCID identification number(s) for the author(s) of this article can be found under https://doi.org/10.1002/admt.201900997.

DOI: 10.1002/admt.201900997

© 2019 WILEY-VCH Verlag GmbH & Co. KGaA, Weinheim

Check for updates
2365709x, 2020, 2, Downloaded from https://onlinelibrary.wiley.com/doi/10.1002/admt.201900997 by Korea Advanced Institute Of, Wiley Online Library on [21/11/2022]. See the Terms and Conditions (https://onlinelibrary.wiley.com/terms-and-conditions) on Wiley Online Library for rules of use; OA articles are governed by the applicable Creative Commons License

Even though the multiresponse actuators that are activated by a combination of Joule heating and humidity[26,27] or light[28,29] have been recently developed for increasing controllability of ETAs, they do not feature the original simplicity and convenience of electrical stimuli-driven actuators.

Another disadvantage of ETAs is their high driving voltage. Generally, carbon nanotubes (CNTs) are frequently employed as a highly aligned conductive material for the heating layer, but their relatively high electrical resistivity necessitates the use of high driving voltages (≈40 V).[30] Even though other conductive materials such as poly(3,4-ethylenedioxythiophene):poly(styren esulfonic acid),[19] laser-reduced graphene oxide (LRGO),[31] and LRGO/Ag nanoparticle composites[32] can be used in place of CNTs, this approach does not solve the problem of high driving voltages. Recently, a promising Ag nanowire (Ag NW)-based ETA with a very low driving voltage (<5 V) has developed.[23] However, the Ag NW embedded multilayers exhibit a weak bonding strength (0.72 N cm^{-1})[33] between actuator multilayers, and can therefore be delaminated during the generation of mechanical stress at the interface. Thus, further development to achieve low driving voltage and robust bonding simultaneously is needed.

Herein, to solve the abovementioned problems, we developed a novel control and design method based on the programming of fabric substrate conductance to implement various actuator shapes. In our previous work,[34] we reported an improved method of fabric spray-coating and found that the conductance of spray-coated fabrics can be controlled. In this work, we controlled the amount of coating solution using a shadow mask to generate a heterogeneous conductance distribution. This heterogeneous conductance distribution allowed us to design the ETA heat distribution and thus control the actuator bending angle. In addition, fabric was used as a porous substrate to simultaneously achieve a low driving voltage and robust bonding. Its porous structure allowed mechanical interlocking of the fabric with polydimethylsiloxane (PDMS) and a chemical bonding of a polyimide (PI) tape with uncured PDMS, while the large surface area of fabric substrate was coated with conductive nanocomposites. The presence of Ag NW/CNT composites allowed the use of low ETA driving voltages of <12 V and high bending stability. Therefore, the heterogeneous conductance (HC)-based locally shape-morphable ETA could be designed and actuated into various shapes with a single substrate geometry at a low driving voltage. Finally, to prove the utility of this actuator for biomimetic soft robotics, we fabricated and successfully tested a self-walking robot capable of crawling on a ratchet surface and demonstrated a practical application of lifting objects in a vacuum chamber.

2. Results and Discussion

2.1. ETA Preparation

ETA operation is based on the mismatch of heating-induced strain in the bipolymer structure due to the CTE difference of the two polymers. In this study, PDMS was used as a high-CTE material for the top layer, and PI tape was used as a low-CTE material for the bottom layer. **Figure 1**a shows a schematic illustration of the fabrication process. As demonstrated in Figure 1a–i, the fabric substrate was spray-coated with a Ag NW/CNT dispersion. After coating, 10% strain was applied to the coated fabric to create microcracks, which allowed uncured PDMS to penetrate the bottom layer of the actuator in the final fabrication stage. After PI tape attachment on the backside of the fabric and the application of a Cu wire electrode (Figure 1a-ii), uncured PDMS was poured onto the substrate in a vacuum chamber, as shown in Figure 1a-iii. At atmospheric pressure, even though the syringe was attached upside down on the chamber ceiling, uncured PDMS could not flow out because of its high viscosity and the relatively low pressure in the syringe. On the contrary, when vacuum was applied, and the pressure in the chamber dropped to below that in the syringe, PDMS began to flow out and coated the fabric. As PDMS was coated after the removal of air bubbles between the fabric and PI tape, it could penetrate the bottom layer of the actuator through microcracks generated during drying. After PDMS curing, the actuator was cut into the designed shape.

The obtained actuator was subjected to peel tests for measuring adhesion strength, a key ETA parameter. Figure S1 of the Supporting Information illustrates the peel test procedure used for four specimens. Sample #2 was fabricated by the abovementioned process, while sample #4 was fabricated by attaching only the PI tape on the fabric. As shown in Figure S2 of the Supporting Information, the adhesion strength of sample #2 was much higher than that of sample #4 (≈4.9-fold) and that of PI tape on cured PDMS[33] (≈7.2-fold), which implies that uncured PDMS, a silicone-based organic polymer, penetrated the porous fabric and engaged in strong chemical bonding with the silicone rubber-containing adhesive layer of the PI tape. This bonding allowed us to fabricate a highly mechanically robust actuator. A more detailed description of the bonding force and cross-sectional images of each sample are provided in Figures S3 and S4 of the Supporting Information.

Figure 1b shows a schematic illustration and photograph of the ETA before and after Joule heating, revealing that this heating induced bending due to the relatively large thermal expansion of PDMS. During the actuation, no defects such as trapped air and delamination were observed on the actuator backside even in the folded and rolled state, as shown in Figure S5 of the Supporting Information. This stability was ascribed to the strong bonding between the adhesive layer of the PI tape and PDMS, and the proposed approach was found to be well suited for the fabrication of strain mismatch-based soft actuators.

2.2. Electrothermal and Electromechanical Characteristics of ETA

Figure 2 shows the electrothermal and electromechanical properties of the proposed ETA. To characterize the actuation performance, we defined the bending angle as the central angle of the arc observed upon actuator bending (Figure 2a). In addition, ETA performance was evaluated in two different situations, namely for the ETA placed on a horizontal table and for the ETA vertically hanged as shown in Figure 2a. According to the initial actuation direction, the former was defined as the +y-direction (+y-ETA) actuator, and the latter

© 2019 WILEY-VCH Verlag GmbH & Co. KGaA, Weinheim

2365709x, 2020, 2, Downloaded from https://onlinelibrary.wiley.com/doi/10.1002/admt.201900997 by Korea Advanced Institute Of, Wiley Online Library on [21/11/2022]. See the Terms and Conditions (https://onlinelibrary.wiley.com/terms-and-conditions) on Wiley Online Library for rules of use; OA articles are governed by the applicable Creative Commons License

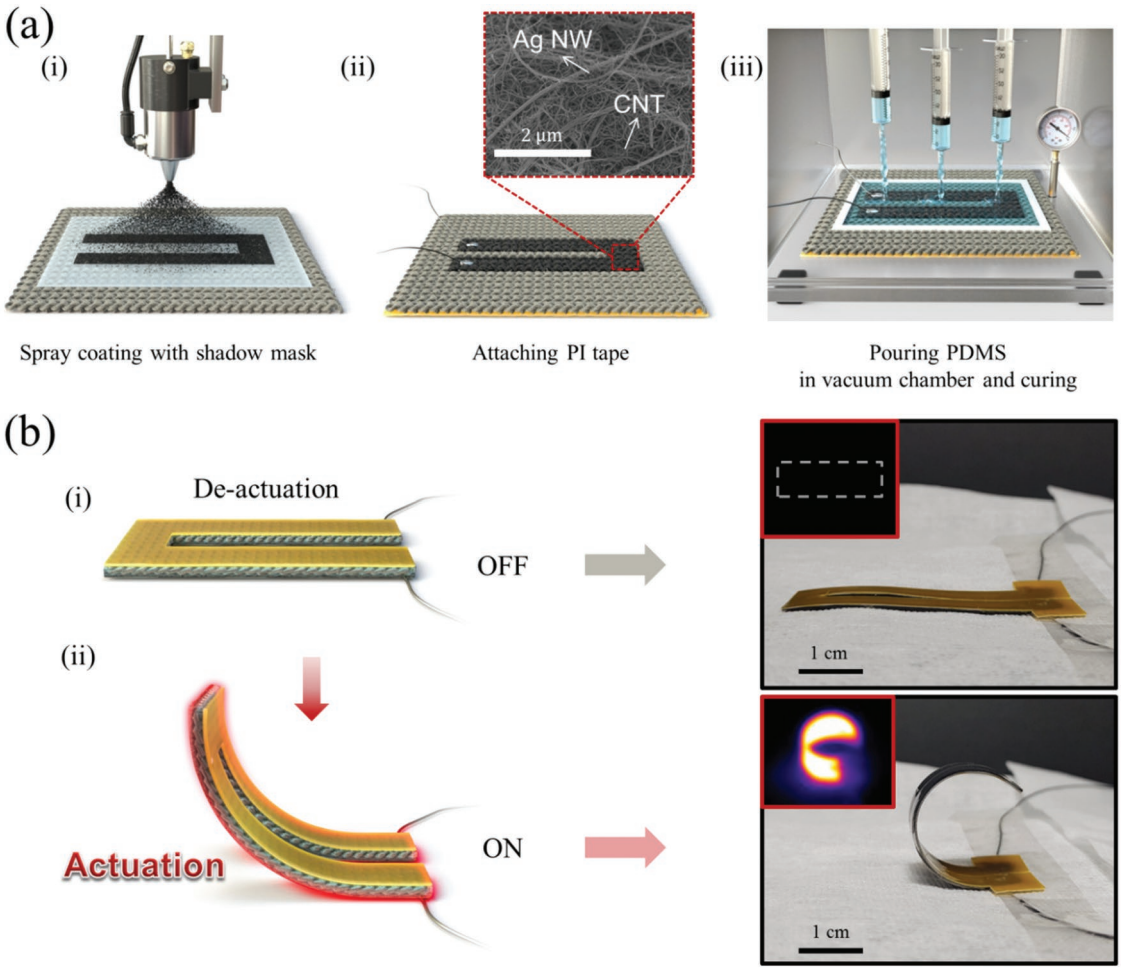


Figure 1. Fabrication of the proposed electrothermal actuator (ETA). a) Schematic illustration of the fabrication process and image of nanocomposite-coated fabric obtained by scanning electron microscopy (SEM). b) Schematics and photographic images of the actuator before/after actuation.

as the $-x$-direction ($-x$-ETA) actuator. Figure 2b shows the bending angle change at an input voltage of 10 V (power consumption: 5.0 W), revealing that the initial response and final bending angle in the $-x$-direction and $+y$-direction were slightly different, while their saturation times were similar. However, the 10–90% response times (τ_{90}) for the $-x$-direction and $+y$-direction were slightly different; 42.0 and 53.6 s, respectively. It is expected that the difference is the result of the effect of heat dissipation and the correlation between actuation force and gravitational force. The saturation was reached, and the maximum bending angle was maintained until the voltage was removed at 140 s, as shown in Videos S1 and S2 of the Supporting Information, with the complete temperature curve shown in Figure S6 of the Supporting Information. Figure 2c,d shows the bending angle change and IR thermal images of $+y$-ETA at different voltages, with further IR and photographic images along the $+y$- and $-x$-directions shown in Figure S7 of the Supporting Information. As shown in the above graph, the bending angle change during actuation at different voltages also depended on the relationship between actuation and gravity force directions, as well as the heat dissipation to the surrounding. Despite this dependence, the voltage-dependent temperature change could be well modeled using the theoretical relationship of $Q = V^2/R$, where Q is the amount of heat, V is the input voltage, and R is the actuator resistance (Figure 2e). Moreover, an on/off cycling test performed at an applied periodical input DC bias voltage of 10 V revealed stable actuator behavior, as shown in Figure 2f and Videos S3 and S4 (Supporting Information).

2.3. ETA Characterization of Samples with Various Conductances

Soft ETAs normally feature a bi-polymer structure, i.e., comprise two polymers with different CTEs. However, the bending of the bipolymer structure is very difficult to model because of the large CTEs and the temperature dependence of material properties such as CTE and Young's modulus.[35] Therefore, to explain the principle of the HC-ETA, we referenced a bimetallic strip structure (Figure S8, Supporting Information). Timoshenko reported that a bimetallic strip uniformly heated along its entire length bends or deforms into an arc of a circle because of the difference between CTEs of the constituent

© 2019 WILEY-VCH Verlag GmbH & Co. KGaA, Weinheim

2365709x, 2020, 2, Downloaded from https://onlinelibrary.wiley.com/doi/10.1002/admt.201900997 by Korea Advanced Institute Of, Wiley Online Library on [21/11/2022]. See the Terms and Conditions (https://onlinelibrary.wiley.com/terms-and-conditions) on Wiley Online Library for rules of use; OA articles are governed by the applicable Creative Commons License

2365709x, 2020, 2, Downloaded from https://onlinelibrary.wiley.com/doi/10.1002/admt.201900997 by Korea Advanced Institute Of, Wiley Online Library on [21/11/2022]. See the Terms and Conditions (https://onlinelibrary.wiley.com/terms-and-conditions) on Wiley Online Library for rules of use; OA articles are governed by the applicable Creative Commons License

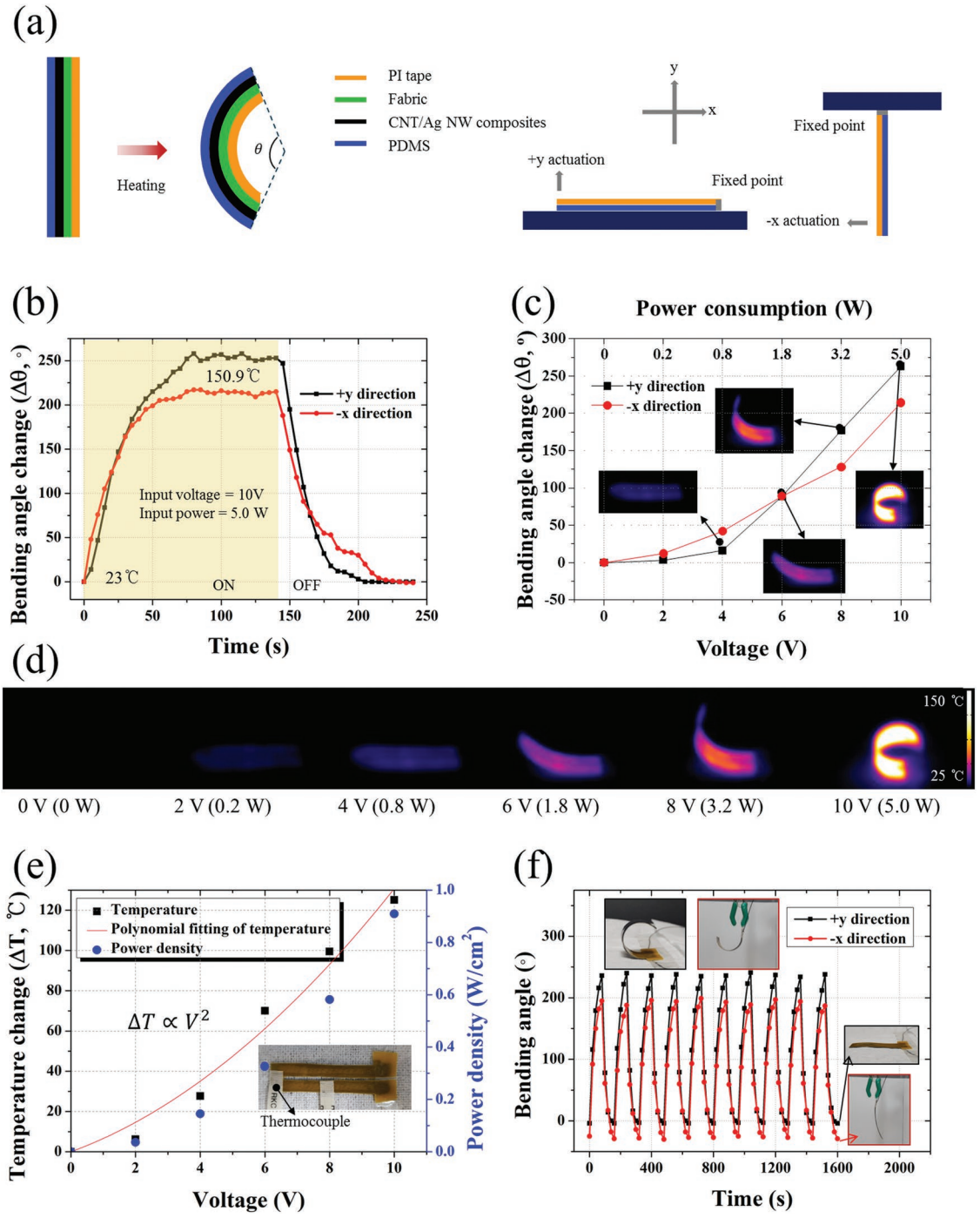


Figure 2. Electromechanical and electrothermal characteristics of the proposed ETA. a) Schematics of the actuation mechanism and definition of actuation directions. b) Time lapse change of bending angles at an input voltage of 10 V. c) Maximal bending angle change as a function of input voltage and d) the corresponding IR thermal images. e) Temperature change and power density of the actuator as a function of voltage. f) Results of the cyclic actuation test for ten periodic cycles at an input voltage of 10 V.

metals.[36] The curvature radius (κ) of the bimetallic strip can be calculated as

$$\kappa = \frac{6E_1E_2(h_1+h_2)h_1h_2(\alpha_1-\alpha_2)\Delta T}{E_1^2h_1^4 + 4E_1E_2h_1^3h_2 + 6E_1E_2h_1^2h_2^2 + 4E_1E_2h_2^3h_1 + E_2^2h_2^4} \quad (1)$$

$$\therefore \kappa \propto \Delta T \,(\text{at constant dimensions}) \quad (2)$$

where T is the temperature, E is the Young's modulus, h is the thickness, α is the CTE, and subscripts 1 and 2 denote materials 1 and 2, respectively. As shown in Equation (2), the curvature radius of the bi-metallic strip is proportional to the temperature change. Therefore, the curvature radius of the bipolymer structure is also expected to be proportional to

 © 2019 WILEY-VCH Verlag GmbH & Co. KGaA, Weinheim

the temperature change despite the difference of the corresponding coefficients. In this study, temperature change is generated by Joule heating, and the relationship between curvature radius and temperature change is expressed as

$$P = \frac{V^2}{R} = V^2 G \tag{3}$$

$$Q(=P) = mc_p \Delta T \tag{4}$$

$$\therefore \kappa \propto \Delta T \propto P \propto G(\text{at constant voltage}) \tag{5}$$

where P is the electric power, R is the electrical resistance, G is the electrical conductance, Q is the added energy, m is the mass of the material, and c_p is the heat capacity. Based on Equation (5), it is concluded that the curvature radius is proportional to the conductance of the bimetallic strip structure for constant dimensions and input voltage. Even though bipolymer structures feature nonlinear actuation due to the change of material properties and large deformation, the actuation tendency can be presumed to resemble that of bimetallic structures.

Figure 3 shows the controllability of sheet resistance and ETA characteristics for different conductance of the heating layer. The sheet resistance of spray-coated fabric was controlled by changing the amount of the coating solution and the Ag NW:CNT weight ratio (Figure 3a), with the corresponding SEM images shown in Figure S9 of the Supporting Information. In this structure, Ag NWs were used as the main material to ensure the electrical conductivity, while CNTs were used as a secondary material for the structural stability. Notably, no electrically conductive network was obtained when only Ag NWs were coated in the absence of CNTs, and optimal results were achieved for a Ag NW:CNT weight ratio of 1:1, as described in our previous work.[34] The lowest electrical conductance with the smallest deviation between the samples was obtained with 0.02:0.02 wt% Ag NW:CNT weight ratio. As shown in Figure 3b, the sheet resistance of the coating layer can be controlled by the amount of coating solution. For example, the sheet resistance was measured as 50.18 Ω sq^{-1} when 10 mL of 0.02:0.02 wt% solution was coated, whereas it was 2.5 Ω sq^{-1} when 50 mL of 0.02:0.02 wt% solution was coated. Therefore, it can be concluded that the bending angle of the actuator can be determined by the electrical conductance of the heating layer, which can be controlled by the amount of coating solution and the Ag NW:CNT weight ratio. Figure 3c shows the maximum ETA curvature as a function of conductance and the corresponding IR and photographic images. The ETA used in this experiment was designed as a 5 cm × 0.5 cm rectangle to allow the application of Equation (5), and conductance was controlled by the amount of coating solution. As the results could be affected by all experimental parameters, various error causes were expected, e.g., electrode weight, uniformity of PDMS thickness, uniformity of spray-coating, and sample dimensions. However, from the graph, it was concluded that the bending curvature of the actuator is approximately proportional to the electrical conductance of the heating layer, following the abovementioned relationship (Equation (5)), with the corresponding bending force for various conductance shown in Figure S10 of the Supporting Information.

2.4. Characterization of the HC-ETA

As mentioned in the Introduction, to make ETAs broadly applicable, various actuation shapes should be possible with low driving voltages. In order to achieve this, the heat distribution in the actuator was controlled by designing the local conductance of the heating layer. **Figure 4** shows the shape-morphing characteristics of the HC-ETA. In this study, two shapes were designed to demonstrate a controllable heterogeneous conductance and heat distribution of HC-ETA. First, a rod-shaped rectangular fabric substrate (5 cm × 0.5 cm) was divided into three zones and coated with a shadow mask to realize the heterogeneous conductance distribution, with a schematic illustration of this process and an electrical model of the rectangular actuator shown in Figure S11a of the Supporting Information. Each part of three zones can be modeled as a resistor, and the power consumption of each zone via Joule heating can be determined by controlling their resistances. In other words, the region with higher resistance consumes higher electrical power, and thus generates larger Joule heating than other regions. To test this model, we designed each part with different conductance, as shown in Figure 4. Here, purple, red, and orange colors indicate the lowest (2.5 Ω sq^{-1}), medium (6.5 Ω sq^{-1}), and the highest (11 Ω sq^{-1}) sheet resistances, respectively. The curvature of each region was calculated by drawing an arc with two end points and the center point of each region. When the HC-ETA was uniformly coated, as shown in Figure 4a-i, it was bent into an arc at an input voltage of 8 V because of the uniform temperature increase of the heater in the longitudinal direction. In this design, the programmed curvature distribution (1:1:1), which was controlled using resistance, was well matched with the experimental results (1:1.05:1.15). By contrast, Figure 4a-ii shows a schematic illustration, an IR thermal image, and a photographic image of a nonuniformly coated center-focused HC-ETA with the central region being less coated to achieve a 2.6-fold lower conductance than those of the side regions. This results in higher power consumption and temperature increase in the central region than the side regions by 2.6-fold. Therefore, the side-regions were with relatively straight line shapes, while the central region was arc-shaped. Here, programmed curvature (1:2.6:1) was well matched with the experimental result (1:2.67:1.05). Moreover, when the central region was more densely coated to achieve a 2.6-fold higher conductance than those of the side regions, the side-region was actuated in a round shape with larger curvature, while the central region was relatively straighter with smaller curvature, as shown in Figure 4a-iii. The overall shape of the fabricated side-focused actuator followed the programmed shape with some difference between the actual curvature ratio (2.84:1:2.91) and the programmed curvature ratio (2.6:1:2.6). In all three cases, small differences between the actual and designed actuation shapes can be ascribed to various factors such as errors in the resistance control and nonuniform

© 2019 WILEY-VCH Verlag GmbH & Co. KGaA, Weinheim

2365709x, 2020, 2, Downloaded from https://onlinelibrary.wiley.com/doi/10.1002/admt.201900997 by Korea Advanced Institute Of, Wiley Online Library on [21/11/2022]. See the Terms and Conditions (https://onlinelibrary.wiley.com/terms-and-conditions) on Wiley Online Library for rules of use; OA articles are governed by the applicable Creative Commons License

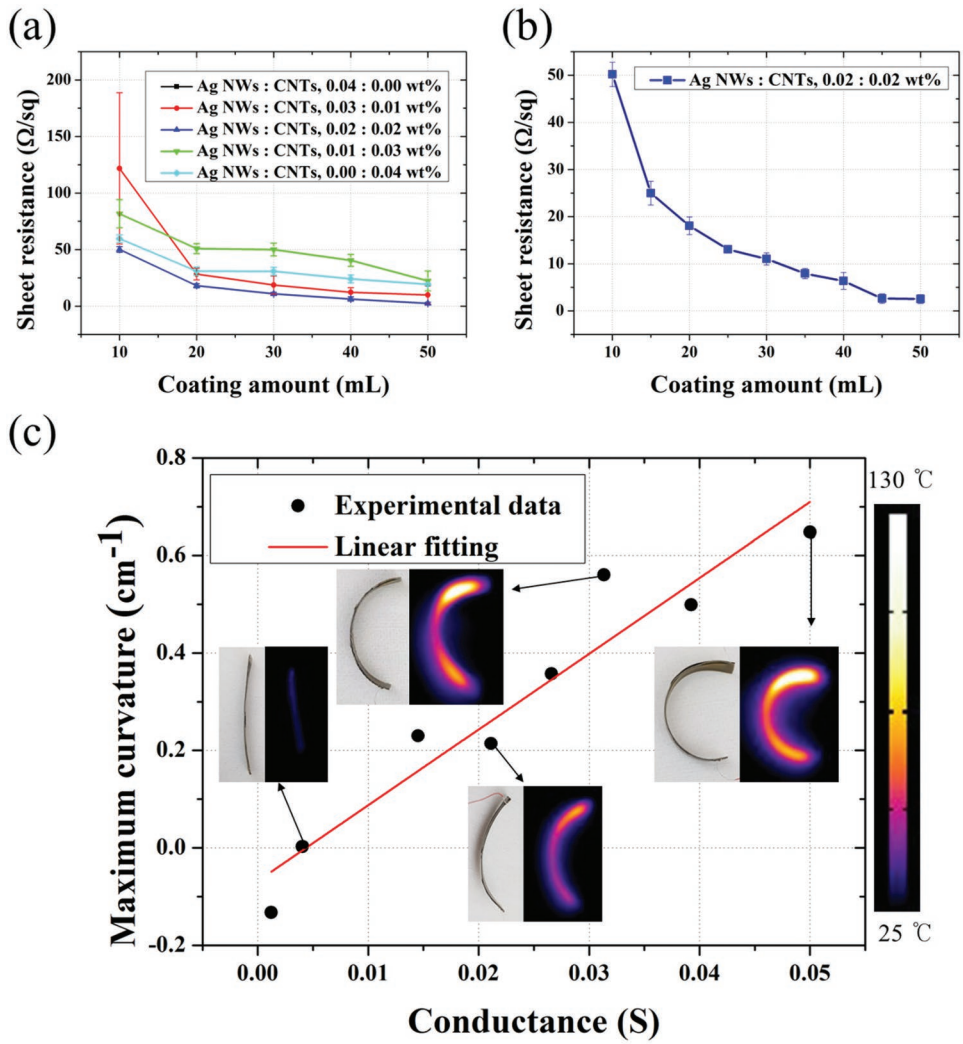


Figure 3. Effects of conductance on actuator properties. a) Dependence of sheet resistance on coating solution volume for different Ag NW:CNT weight ratios. b) Effect of coating solution volume on the sheet resistance of the optimized solution-coated fabric. c) Maximum curvature as a function of actuator conductance at a constant input voltage of 10 V.

weight and stiffness due to the Ag paste and interconnection wires at the boundary.

Second, an X-shaped fabric substrate (dimensions are specified in Figure S11b, Supporting Information) was divided into five regions, and an electrode was placed at each end point of the actuator (Figure S11b, Supporting Information). As the temperature change of each region is proportional to the surface power density (i.e., power consumption per area), the temperature change of uniformly coated actuator could be calculated as follows

$$\text{Let } R_a = R_1 = R_2 = R_4 = R_5,\ R_b = R_3 \tag{6}$$

$$P_a \approx \frac{R_a V^2}{4\left(8R_a + R_b\right)^2},\ P_b \approx \frac{R_b V^2}{\left(8R_a + R_b\right)^2} \tag{7}$$

$$Q_a = \frac{P_a}{A_a},\ Q_b = \frac{P_b}{A_b} \tag{8}$$

$$\text{If) } R_a = R_b \tag{9}$$

$$4 \times Q_a \approx Q_b \tag{10}$$

$$4 \times \Delta T_a \approx \Delta T_b \tag{11}$$

where subscript "*a*" refers to the unit cell of the side regions and subscript "*b*" refers to the unit cell of the central region, R is the electrical resistance of the unit cell, as shown in Figure S11b of the Supporting Information, P is the dissipated power, Q is the surface power density, A is the unit cell area (0.5 cm × 0.5 cm), V is the input voltage, and T is the temperature. In the above equation, R is proportional to sheet resistance when the width is constant and the resistor thickness variation is uniform or negligible. Therefore, Equation (11) suggests that the temperature change of the central part would be four times larger than that of the side regions. Figure 4b–i shows a schematic illustration of the spray-coating process with an X-shaped

© 2019 WILEY-VCH Verlag GmbH & Co. KGaA, Weinheim

2365709x, 2020, 2, Downloaded from https://onlinelibrary.wiley.com/doi/10.1002/admt.201900997 by Korea Advanced Institute Of, Wiley Online Library on [21/11/2022]. See the Terms and Conditions (https://onlinelibrary.wiley.com/terms-and-conditions) on Wiley Online Library for rules of use; OA articles are governed by the applicable Creative Commons License

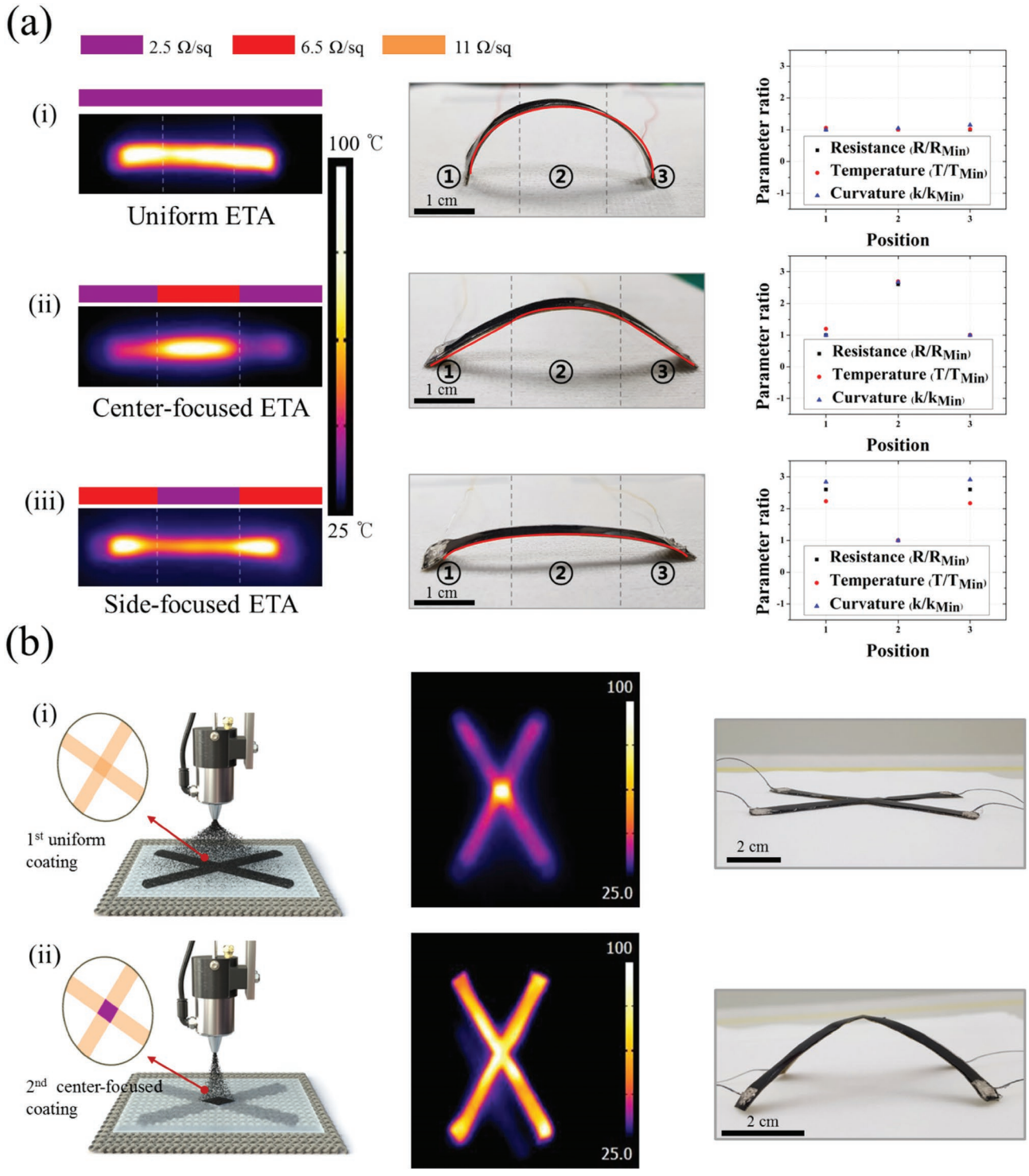


Figure 4. Characterization of the heterogeneous conductance-based locally shape-morphable electrothermal actuator. a) IR thermal images and photographs of the rod-shaped actuator, and the relationship between the parameters of (i) a uniform actuator, (ii) a center-focused actuator, and (iii) a side-focused actuator at an applied voltage of 8 V (power consumption: 2.56, 1.7, and 1.3 W, respectively). b) Schematic illustration of the spray-coating process, IR images, and photographs of the X-shaped actuator (i) uniformly coated at an applied voltage of 15 V (power consumption: 4.5 W) and (ii) center-focused coated for uniform heat distribution at an applied voltage of 25 V (power consumption: 12.5 W).

shadow mask. As the corresponding conductance distribution was uniform, a nonuniform heat distribution was observed at an input voltage of 15 V (Figure 4b–i). When current flow was crossed in the central part, heat was concentrated at the crossing point, as calculated by Equation (11), and no actuation could occur (Figure 4b–i). The resistances of each region

© 2019 WILEY-VCH Verlag GmbH & Co. KGaA, Weinheim

2365709x, 2020, 2, Downloaded from https://onlinelibrary.wiley.com/doi/10.1002/admt.201900997 by Korea Advanced Institute Of, Wiley Online Library on [21/11/2022]. See the Terms and Conditions (https://onlinelibrary.wiley.com/terms-and-conditions) on Wiley Online Library for rules of use; OA articles are governed by the applicable Creative Commons License

required to obtain a uniform heat distribution were calculated as follows

$$\text{For } Q_a = Q_b \tag{12}$$

$$R_b \approx \frac{R_a}{4} \tag{13}$$

Equation (13) suggests that for a uniform heat distribution, sheet resistance at the center should be four times smaller than that at the side. Therefore, spray-coating was conducted in two steps. After the whole region was coated using an X-shaped mask, the central region was coated again using a shadow mask to achieve higher conductance (Figure 4b–ii). Figure 4b–ii shows an IR image of the actuator heated at a bias of 25 V, and the observed temperature uniformity reveals that the experimental result matches well with the theoretical modeling. Finally, successful thermal actuation of the X-shaped actuator was accomplished, as shown in the photographic image of the actuator in Figure 4b–ii.

2.5. Application of the HC-ETA as a Biomimetic Self-Walking Robot and a Soft Robot

The HC-ETA was utilized to fabricate a lightweight and biomimetic self-walking robot as presented in **Figure 5**a. Here, uniformly coated rod-shaped actuator shown in Figure 4a–i was used for the self-walking robot. For the one directional walking motion of the self-walking robot, periodic electrical voltage pulses were supplied to the actuator and a rough surface with asymmetrical ratchet structures was employed (see Figure S12, Supporting Information). When periodic pulses of voltage were applied to the HC-ETA, the rear leg of the rod-shaped self-walking robot slid over the long side of the sawtooth-shaped ground, as shown in Figure 5a, while the steep side of this ground prevented the front leg from moving backward. By contrast, when the voltage was released, the front leg moved forward over the long side of the sawtooth, and the rear leg stayed in the same position. This mechanism allowed the self-walking robot to move in the forward direction along the ratchet surface with periodic voltage pulses. Figure 5a shows the photographic and IR thermal images captured during the self-walking process. The initial state before actuation is shown in Figure 5a–i, while the corresponding IR image is black, as the actuator was at room temperature. After actuation, the self-walking robot was heated and bent into an arc shape, as shown in Figure 5a–ii. Through the middle stage (Figure 5a–iii) with worm-like crawling motion, the walker reached the end of the ratchet ground with a walking speed of 15 mm min^{-1} (Figure 5a–iv), as shown in Video S5 of the Supporting Information.

In addition to the self-walking soft robot, the HC-ETA can also be used for object lifting functions. Here, we designed a second X-shaped actuator that can be driven at low voltage (12 V) by changing the electrode positions; details of the calculation process are provided in Figure S13 of the Supporting Information. Figure 5b shows a schematic of the dip-coating process performed using the X-shaped actuator. A piece of paper was hung on the actuator in a vacuum chamber with a silver nanoparticle solution placed under it. In the initial state, the paper hovered in the air due to the actuation of the HC-ETA and did not come into contact with the solution, as shown in Figure 5b–i. Deactuation, which resulted in the paper dipping into the solution, was conducted after the air was removed, as shown in Figure 5b–ii. When the paper was removed from the solution upon the reapplication of actuation voltage, as shown in Figure 5b–iii, one cycle of dip-coating was completed. Notably, even after the paper was dipped into the solution and had absorbed the silver nanoparticle solution, the actuator exerted a force sufficient to overcome the drag force on the paper as it moved out of the solution, as shown in Video S6 of the Supporting Information. Another lifting application of the X-shaped actuator was also suggested. Figure 5c shows the process by which a sponge in a vacuum chamber is lifted. When voltage was applied, the actuator lifted the sponge (weight = 0.9 g), as shown in Video S7 of the Supporting Information. These demonstrations revealed that the developed actuator can exert a force sufficient to lift lightweight objects or overcome the drag force during film dip-coating and is therefore well suited for practical applications such as in object-lifting soft robots.

3. Conclusion

In summary, we have developed a novel method of ETA design that allows the actuator to be locally shape-controlled. In this study, we found that the bending curvature of ETA can be controlled in proportion to the electrical conductance of an actuator under constant bias voltage. Accordingly, heterogeneous conductance distribution of the ETA was designed using electrical modeling and implemented by adjusting the coating density of a conductive material for local shape control. Moreover, the unique characteristics of the fabric substrate used were shown to apply well to the fabrication of a soft actuator. The porous and woven structure of the fabric allowed us to simultaneously achieve both thick nanomaterial coating for high electrical conductivity and strong bonding of multilayers for mechanical stability. Consequently, the developed actuator could be driven by low voltages (<12 V) and was well suited for various applications such as a biomimetic self-walking robot and an object lifting flexible robot. Within our knowledge, this is the first actuator design method of shape controllable ETA via heterogeneous conductance distribution, and we believe that the developed method can be viewed as a benchmark for subsequent research. Furthermore, the proposed design and fabrication methods are believed to contribute to the use of ETAs in real-life applications such as soft robotics, artificial muscles, and biomedical devices.

4. Experimental Section

Fabrication of ETA: The spray-coating process was largely based on the previous work. Multiple walled CNTs (Hanwha, Korea) were mixed with isopropyl alcohol (IPA, Sigma-Aldrich, Korea) to achieve a loading of 0.02 wt%; the resulting mixture was subjected to sonication for 10 min (VCX-130 tip sonicator, Sonics and Materials, USA).

© 2019 WILEY-VCH Verlag GmbH & Co. KGaA, Weinheim

2365709x, 2020, 2, Downloaded from https://onlinelibrary.wiley.com/doi/10.1002/admt.201900997 by Korea Advanced Institute Of, Wiley Online Library on [21/11/2022]. See the Terms and Conditions (https://onlinelibrary.wiley.com/terms-and-conditions) on Wiley Online Library for rules of use; OA articles are governed by the applicable Creative Commons License

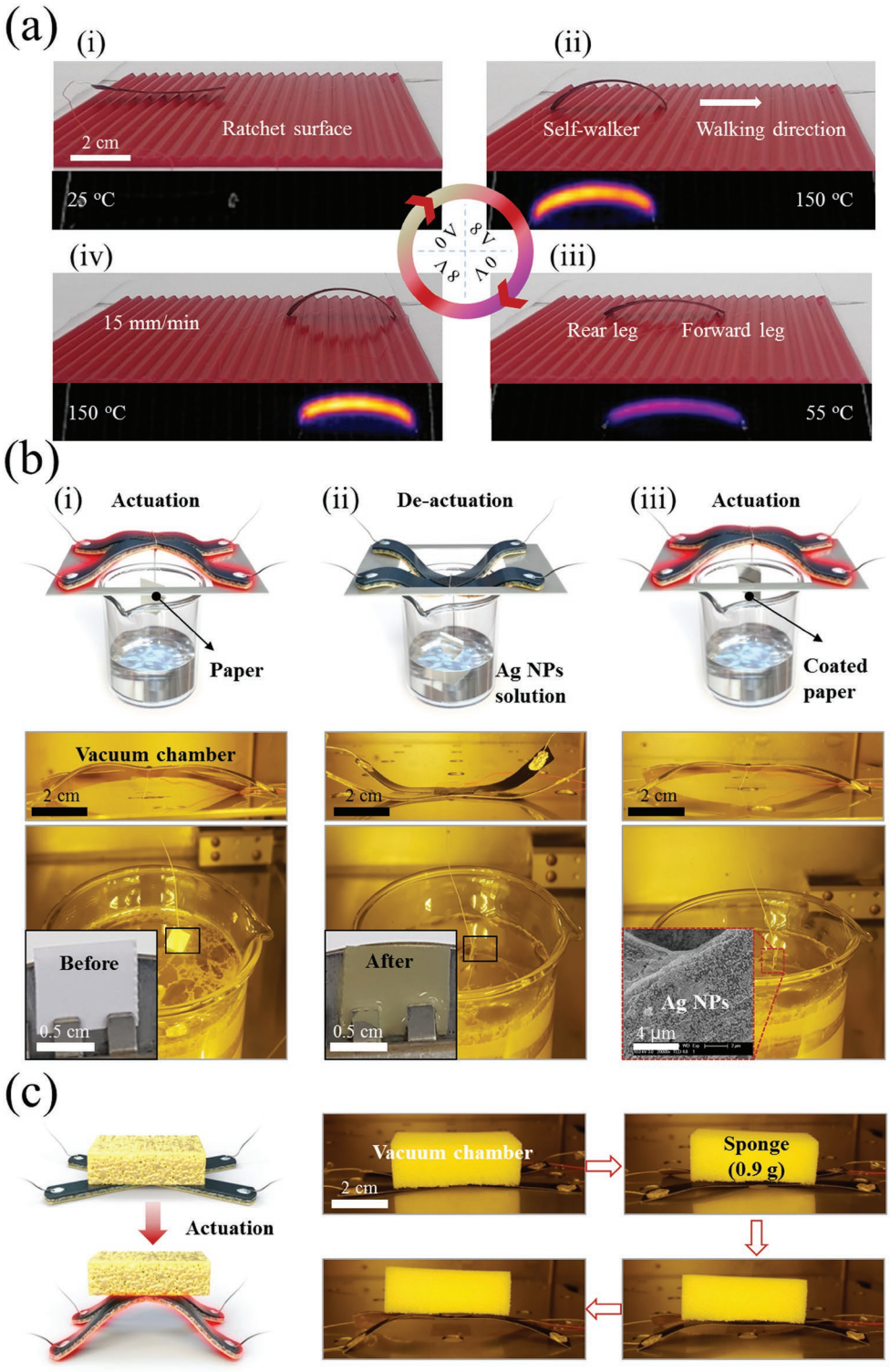


Figure 5. Application of the rod-shaped actuator as a self-walking robot and the X-shaped actuator as a soft robot in a vacuum chamber. a) Photographs and infrared thermal images for all steps taken by the self-walking robot (walking velocity = 15 mm min^{-1}). b) Schematics and photographs of the dip-coating process. Insets show photographs of the paper before/after it is dipped into the solution, and the red dotted box shows an SEM image of the dip-coated paper. c) Schematic and photograph of the lifting process. A driving voltage of 12 V was used in all cases.

The sonication process comprised a series of 3 s injections followed by 1 s rest periods to prevent the thermally induced aggregation of CNTs. The obtained dispersion was mixed with an Ag NW solution (UniNano Tech, Korea) to achieve an Ag NW loading of 0.02 wt%, sonicated for 5 min as described above, and allowed to cool to room temperature for 30 min.

© 2019 WILEY-VCH Verlag GmbH & Co. KGaA, Weinheim

2365709x, 2020, 2, Downloaded from https://onlinelibrary.wiley.com/doi/10.1002/admt.201900997 by Korea Advanced Institute Of, Wiley Online Library on [21/11/2022]. See the Terms and Conditions (https://onlinelibrary.wiley.com/terms-and-conditions) on Wiley Online Library for rules of use; OA articles are governed by the applicable Creative Commons License

The resulting dispersion was spray-coated (EFD 781S, Nordson EFD, Korea) on a 3 cm × 9 cm piece of fabric substrate (81% polyethylene, 19% spandex) using a 3D-printed shadow mask. A regulator pressure of 0.05 MPa and a round pattern nozzle (#7857-46SS, Nordson EFD, Korea) were used. To make microsize cracks, a 10% strain was applied to the fabric during the drying process. After spray-coating was completed, polyimide (PI) tape (Dupont, USA) was attached to the back of the fabric and the coated side was fitted with a Cu wire using Ag paste as a conductive adhesive. Finally, a liquid silicone rubber precursor (Sylgard 184, Sigma-Aldrich, USA) was poured onto the sample in a vacuum chamber. Syringes containing uncured PDMS were fixed to the ceiling of the vacuum chamber with their tips facing downward. When the air in the chamber was removed, the uncured PDMS was squeezed out onto the fabric substrate because of the difference in pressure, which allowed any air bubbles between the fabric and PI tape to be completely removed. The PDMS-impregnated sample was cured at 50 °C in a convection oven for 24 h and cut into the shape designed.

Characterization of ETA: During the experiments with the fabricated actuator, the temperature was recorded by a data logger (midi LOGGER GL220, Graphtec, Japan). Its thermocouples were attached to the PI tapes of ETA as shown in Figure 2e and the average temperature of each point was used to characterize the ETA. For the bending angle measurements, videos of all bending tests were recorded, and the captured images were imported into Autocad (Autodesk, USA). The voltage was applied utilizing a power supply (UP-3005D, Unicorn TMI, Korea), and IR thermal imaging was performed using an IR thermal camera (E6, FLIR Systems, USA).

Characterization of the Variable-Conductance ETA: The solution of CNTs was mixed with Ag NWs in IPA solution to achieve Ag NW:CNT weight ratios of 0:4, 1:3, 2:2, 3:1, and 4:0. For each ratio, 10, 20, 30, 40, and 50 mL of the solution was coated onto a 3 cm × 3 cm fabric substrate, and the prepared samples were characterized via SEM (Sirion, FEI Co., The Netherlands) and sheet resistance measurements (FPP-2400 four-point probe, Dasol Eng, Korea). For the latter five portions of the same sample were examined. The optimized composition for the coating solution was identified as 0.02 wt% CNTs and 0.02 wt% Ag NWs, and the corresponding solution was used to fabricate actuators.

Fabrication of Rod- and X-Shaped Actuators: A rod-shaped 5 cm × 0.5 cm rectangular actuator was fabricated using two-step spray-coating. First, the entire fabric was spray-coated with the above solution using a rod-shaped shadow mask, and to achieve a partial conductance difference, the solution was spray-coated again using a patterned shadow mask. An X-shaped actuator was fabricated using similar procedure. In this case, instead of the rod-shaped shadow mask, an X-shaped shadow mask was used for the first spray-coating, and a rhombus-shaped mask was used for the second spray-coating in the crossing region.

Self-Walking Robot Fabrication and Actuation Testing in a Vacuum Chamber: The self-walking robot, which was designed in the same way as the uniform rod-shaped actuator in Figure 4a–i, had a sheet resistance of 2.5 Ω sq^{-1}, and the ratchet surface was made using a 3D printer. The self-walking robot was placed on the ratchet surface and periodical input voltage of 10 V was applied to wake it. The object lifting actuator was fabricated using similar procedure with X-shaped actuator in Figure 4b–ii except the position of electrodes. To lower the driving voltage, the ground at each edge of the X-shaped actuator and the positive potential at center were applied, with details of the calculation and design provided in Figure S13 of the Supporting Information. For the dip-coating test in the vacuum chamber, a piece of paper (Double A, Thailand) was hung at the center of the X-shaped actuator using thin wire and dipped into an Ag nanoparticle solution (0.05 wt%) dispersed in deionized water. For the lifting test, lightweight sponge (weight = 0.9 g) was placed onto the center of the developed X-shaped actuator. During these experiments, the vacuum in the chamber was maintained at 0.8 bar.

Supporting Information

Supporting Information is available from the Wiley Online Library or from the author.

Acknowledgements

This work was supported by the Center for Advanced Meta-Materials (CAMM) funded by the Ministry of Science, ICT and Future Planning as Global Frontier Project (CAMM No. 2014M3A6B3063707), and by the National Research Foundation of Korea (NRF) grant funded by the Korea government (MSIT) (No. 2018R1A2B2004910).

Conflict of Interest

The authors declare no conflict of interest.

Keywords

electrothermal actuators, nanocomposites, shape morphing, soft actuators, textiles

Received: November 5, 2019
Revised: November 26, 2019
Published online: December 11, 2019

[1] L. Hines, K. Petersen, G. Z. Lum, M. Sitti, *Adv. Mater.* **2017**, *29*, 1603483.
[2] I. K. Han, T. Chung, J. Han, Y. S. Kim, *Nano Convergence* **2019**, *6*, 18.
[3] C. Yoon, *Nano Convergence* **2019**, *6*, 20.
[4] L. Belding, B. Baytekin, H. T. Baytekin, P. Rothemund, M. S. Verma, A. Nemiroski, D. Sameoto, B. A. Grzybowski, G. M. Whitesides, *Adv. Mater.* **2018**, *30*, 1.
[5] M. T. Tolley, R. F. Shepherd, B. Mosadegh, K. C. Galloway, M. Wehner, M. Karpelson, R. J. Wood, G. M. Whitesides, *Soft Rob.* **2014**, *1*, 213.
[6] J. Hu, X. Li, Y. Ni, S. Ma, H. Yu, *J. Mater. Chem. C* **2018**, *6*, 10815.
[7] S. Banisadr, J. Chen, *Sci. Rep.* **2017**, *7*, 17521.
[8] L. Dong, X. Tong, H. Zhang, M. Chen, Y. Zhao, *Mater. Chem. Front.* **2018**, *2*, 1383.
[9] H. Zeng, P. Wasylczyk, D. S. Wiersma, A. Priimagi, *Adv. Mater.* **2018**, *30*, 1703554.
[10] H. Lee, C. Xia, N. X. Fang, *Soft Matter* **2010**, *6*, 4342.
[11] R. Fuhrer, E. K. Athanassiou, N. A. Luechinger, W. J. Stark, *Small* **2009**, *5*, 383.
[12] X. Zhao, S. A. Chester, H. Yuk, R. Zhao, Y. Kim, *Nature* **2018**, *558*, 274.
[13] W. Hu, G. Z. Lum, M. Mastrangeli, M. Sitti, *Nature* **2018**, *554*, 81.
[14] Y. F. Zhang, N. Zhang, H. Hingorani, N. Ding, D. Wang, C. Yuan, B. Zhang, G. Gu, Q. Ge, *Adv. Funct. Mater.* **2019**, *29*, 1970098.
[15] Y. Wu, J. K. Yim, J. Liang, Z. Shao, M. Qi, J. Zhong, Z. Luo, X. Yan, M. Zhang, X. Wang, R. S. Fearing, *Sci. Rob.* **2019**, *4*, eaax1594.
[16] C. Yang, W. Wang, C. Yao, R. Xie, X. J. Ju, Z. Liu, L. Y. Chu, *Sci. Rep.* **2015**, *5*, 13622.
[17] Y. Yan, T. Santaniello, L. G. Bettini, C. Minnai, A. Bellacicca, R. Porotti, I. Denti, G. Faraone, M. Merlini, C. Lenardi, P. Milani, *Adv. Mater.* **2017**, *29*, 1606109.
[18] N. Besse, S. Rosset, J. J. Zarate, H. Shea, *Adv. Mater. Technol.* **2017**, *2*, 1700102.
[19] M. M. Hamedi, V. E. Campbell, P. Rothemund, F. Güder, D. C. Christodouleas, J. F. Bloch, G. M. Whitesides, *Adv. Funct. Mater.* **2016**, *26*, 2446.
[20] Y. Hu, T. Lan, G. Wu, Z. Zhu, W. Chen, *Nanoscale* **2014**, *6*, 12703.
[21] Q. Li, C. Liu, Y. H. Lin, L. Liu, K. Jiang, S. Fan, *ACS Nano* **2015**, *9*, 409.
[22] Q. Li, C. Liu, S. Fan, *Nanotechnology* **2018**, *29*, 175503.

© 2019 WILEY-VCH Verlag GmbH & Co. KGaA, Weinheim

2365709x, 2020, 2, Downloaded from https://onlinelibrary.wiley.com/doi/10.1002/admt.201900997 by Korea Advanced Institute Of, Wiley Online Library on [21/11/2022]. See the Terms and Conditions (https://onlinelibrary.wiley.com/terms-and-conditions) on Wiley Online Library for rules of use; OA articles are governed by the applicable Creative Commons License

[23] S. Yao, J. Cui, Z. Cui, Y. Zhu, *Nanoscale* **2017**, *9*, 3797.
[24] H. Kim, H. Lee, I. Ha, J. Jung, P. Won, H. Cho, J. Yeo, S. Hong, S. Han, J. Kwon, K. J. Cho, *Adv. Funct. Mater.* **2018**, *28*, 1801847.
[25] X. Q Wang, C. F. Tan, K. H. Chan, X. Lu, L. Zhu, S. W. Kim, G. W. Ho, *Nat. Commun.* **2018**, *9*, 3438.
[26] J. Li, L. Mou, R. Zhang, J. Sun, R. Wang, B An, H. Chen, K. Inoue, R. Ovalle-Robles, Z. Liu, *Carbon* **2019**, *148*, 487.
[27] M. Amjadi, M. Sitti, *ACS Nano* **2016**, *10*, 10202.
[28] L. Yang, K. Qi, L. Chang, A. Xu, Y. Hu, H. Zhai, P. Lu, *J. Mater. Chem. B* **2018**, *6*, 5031.
[29] Y. Hu, J. Liu, L. Chang, L. Yang, A. Xu, K. Qi, P. Lu, G. Wu, W. Chen, Y. Wu, *Adv. Funct. Mater.* **2017**, *27*, 1704388.
[30] Z. W. Zhou, Q. H. Yan, C. H. Liu, S. S. Fan, *New Carbon Mater.* **2017**, *32*, 411.
[31] T. Y. Zhang, Q. Wang, N. Q. Deng, H. M. Zhao, D. Y. Wang, Z. Yang, Y. Liu, Y. Yang, T. L. Ren, *Appl. Phys. Lett.* **2017**, *111*, 121901.
[32] Q. Wang, Y. T. Li, T. Y. Zhang, D. Y. Wang, Y. Tian, J. C. Yan, H. Tian, Y. Yang, F. Yang, T. L. Ren, *Appl. Phys. Lett.* **2018**, *112*, 133902.
[33] M. V. Hoang, H. J. Chung, A. L. Elias, *J. Micromech. Microeng.* **2016**, *26*, 105019.
[34] J. Ahn, J. Gu, B. Hwang, H. Kang, S. Hwang, S. Jeon, J. H. Jeong, I. Park, *Nanotechnology* **2019**, *30*, 455707.
[35] Y. H. Zhao, Z. K. Wu, S. L. Bai, *Composites, Part A* **2015**, *72*, 200.
[36] B. Y. S. Timoshenko, *J. Opt. Soc. Am.* **1925**, *11*, 233.

 © 2019 WILEY-VCH Verlag GmbH & Co. KGaA, Weinheim

2365709x, 2020, 2, Downloaded from https://onlinelibrary.wiley.com/doi/10.1002/admt.201900997 by Korea Advanced Institute Of, Wiley Online Library on [21/11/2022]. See the Terms and Conditions (https://onlinelibrary.wiley.com/terms-and-conditions) on Wiley Online Library for rules of use; OA articles are governed by the applicable Creative Commons License